

Journal of Intelligent Material Systems and Structures

<http://jim.sagepub.com/>

Performance analysis of a harmonica-type aeroelastic micropower generator

Amin Bibo, Gang Li and Mohammed F Daqaq

Journal of Intelligent Material Systems and Structures 2012 23: 1461 originally published online 15 March 2012

DOI: 10.1177/1045389X12438625

The online version of this article can be found at:

<http://jim.sagepub.com/content/23/13/1461>

Published by:



<http://www.sagepublications.com>

Additional services and information for *Journal of Intelligent Material Systems and Structures* can be found at:

Email Alerts: <http://jim.sagepub.com/cgi/alerts>

Subscriptions: <http://jim.sagepub.com/subscriptions>

Reprints: <http://www.sagepub.com/journalsReprints.nav>

Permissions: <http://www.sagepub.com/journalsPermissions.nav>

Citations: <http://jim.sagepub.com/content/23/13/1461.refs.html>


>> [Version of Record](#) - Aug 24, 2012

[OnlineFirst Version of Record](#) - Mar 15, 2012

[What is This?](#)

Performance analysis of a harmonica-type aeroelastic micropower generator

Amin Bibo, Gang Li and Mohammed F Daqaq

Journal of Intelligent Material Systems and Structures
23(13) 1461–1474
© The Author(s) 2012
Reprints and permissions:
sagepub.co.uk/journalsPermissions.nav
DOI: 10.1177/1045389X12438625
jim.sagepub.com


Abstract

This article investigates the influence of the design parameters on the performance of an aeroelastic micropower generator with the goal of minimizing its cut-in wind speed and maximizing its output power. The generator, which mimics the basic physics of music-playing harmonicas, transforms wind energy into electricity via the self-excited oscillations of a piezoelectric reed embedded within a cavity. Previously, the authors have presented and validated an analytical aeroelectromechanical model describing the response behavior of the generator. By utilizing the proposed model, this study implements a stability analysis and numerical optimization algorithms to delineate the influence of the design parameters on the device's response. The effect of the electric load, chamber volume, and aperture size on the cut-in wind speed is investigated. The results illustrate that the cut-in wind speed can be reduced significantly if the device is designed with an optimal chamber volume, which is shown to be inversely proportional to the square of the beam's first modal frequency. Minimizing the aperture width is also shown to significantly reduce the cut-in speed. However, due to the reduced strain rate in the piezoelectric layer, it is observed that minimizing the wind speed does not always yield an increase in the output power. As such, a numerical investigation of the influence of the design parameters on the output power is utilized to generate design charts that assist in the selection of the optimal parameters for a known average wind speed. Several qualitative verifications of the theoretical trends are also presented through an experimental case study.

Keywords

micropower generator, aeroelastic, Hopf bifurcation, cut-in speed

Introduction

During the last decade, many new concepts for micropower generation have been introduced and exploited to harness wasted energy (e.g. solar, mechanical, and wind) from the environment. These energy harvesters, also known as micropower generators (MPGs), aim to produce small amounts of supplemental power to recharge batteries or to maintain and allow autonomous operation of remote low-power consumption sensors among other electronic devices. Their actual value lies in their ability to regularly generate power with the key features of scalability, design simplicity, high-power density, and low cost.

In recent years, MPGs that utilize flow-induced oscillations of piezoelectric and ferromagnetic structures have been gaining significant interest (Allen and Smits, 2001; Barrero-Gil et al., 2010; Bryant and Garcia, 2011; Kinsey and Dumas, 2008; Liao et al., 2003; Robbins et al., 2006; Simpson et al., 2008; Tang et al., 2009; Zhu et al., 2009). Such designs are currently being exploited as a possible replacement for traditional microwind turbines, which implement rotary-type electromagnetic generators. Rotary designs have been

shown to have scalability issues due to the relatively high viscous drag at low Reynolds numbers, bearing and thermal losses that increase significantly as size decreases, and high electromagnetic interferences (Lissaman, 1983). Additionally, the design and fabrication of small-scale rotary generators that require a rotor, a stator, magnets, wirings, and blades have proved to be very complex and expensive.

The research on utilizing flow-induced oscillations for energy generation has arguably started with the work of Allen and Smits (2001) who investigated the feasibility of placing a piezoelectric membrane in the wake of a bluff body and using the induced oscillations due to the formed vortex street behind the body

Nonlinear Vibrations and Energy Harvesting Laboratory (NOVEHL),
Department of Mechanical Engineering, Clemson University, Clemson,
SC, USA

Corresponding author:

Mohammed F Daqaq, Nonlinear Vibrations and Energy Harvesting
Laboratory (NOVEHL), Department of Mechanical Engineering, Clemson
University, 204 Flour Daniel Bldn, Clemson, SC 29634, USA.
Email: mdaqaq@clemson.edu

to provide a power source. This initial work has been followed by several studies including that of Tang et al. (2009) who developed a flutter mill, which consists of a two-dimensional cantilevered flexible plate mounted in axial flow. Kinsey and Dumas (2008) investigated the concept of power extraction from oscillating wing using unsteady two-dimensional laminar-flow simulations. Zhu et al. (2009) also investigated the performance of a flow-energy harvester based on oscillating foils. De Marqui et al. (2010) investigated the concept of a generator wing with both continuous and segmented electrodes using a finite element analysis combined with an unsteady aerodynamic model. In other demonstrations, Erturk et al. (2010) experimentally investigated the potential of utilizing fluid structural interactions to harvest energy from ambient air using cantilevered beams; and Dunnmon et al. (2011) studied the nonlinear aeroelastic response of an energy-harvesting plate with piezoelectric laminates.

Along the same lines, the authors (Bibo et al., 2010; St Clair et al., 2010) have introduced a new concept for an aeroelastic generator, which transforms wind energy into electricity via wind-induced self-excited oscillations of a piezoelectric beam, as shown in Figure 1(a). The device consists of a piezoelectric cantilever unimorph structure embedded within a cavity to mimic the vibrations of the reeds in a harmonica when subjected to air-flow. As shown in Figure 1, when the air of inflow rate U_0 blows into the chamber of volume V_r , it produces a

pressure $P_A(t)$ on the beam's surface and tries to escape through a small gap, b , between the cantilever and the supporting structure. This, in turn, produces a pressure drop across the cantilever forcing the beam to bend outward and increasing the aperture area. Consequently, the flow velocity through the aperture drops, and the pressure drop across the beam decreases. The mechanical restoring force pulls the beam back decreasing the aperture area, and the process is repeated. Periodic fluctuations in the pressure cause the beam to undergo self-sustained oscillations that produce a time-varying strain in the piezoelectric layer. The piezoelectric element transforms the strain into an alternating voltage, $V(t)$, across an electric load, R .

The onset of self-excited oscillations occurs when the volume flow rate U_0 is large enough such that the energy pumped into the structure via nonlinear pressure forces offsets the intrinsic damping in the system that consists of the structural damping and electric damping due to electric energy generation. This process can be explained as a nonlinear feedback mechanism in which the motion of the cantilever produces a disturbance in the potential flow that feeds enough energy back to the structure to overcome the internal damping (Fletcher, 1992; Hilaire, 1976; Tarnopolsky et al., 2000, 2001).

Using a combination of basic theories in continuous-system vibrations, piezoelectricity, and fluid dynamics, the authors have developed and experimentally

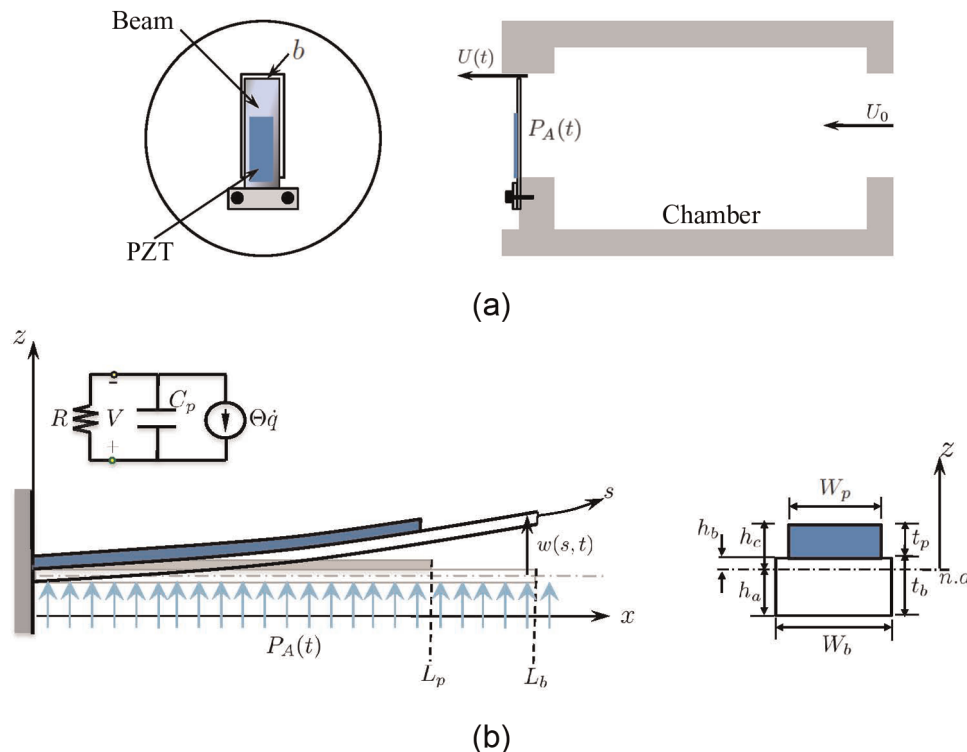


Figure 1. Schematic representation of the proposed aeroelastic MPG.

(a) sectional view, and (b) beam harvester schematic. MPG: micropower generator; PZT: lead zirconate titanate.

validated an analytical aeroelectromechanical model to predict the response behavior of the self-excited MPG (Bibo et al., 2010). A reduced-order model was found to take the form

$$\ddot{q}(t) + 2\zeta\omega\dot{q}(t) + \omega^2q(t) + \Theta V(t) = \mathcal{E}P_A(t) \quad (1)$$

$$\dot{V}(t) + \frac{V(t)}{RC_p} = \frac{\Theta}{C_p}\dot{q}(t) \quad (2)$$

$$\dot{P}_A(t) = \frac{\rho_a c^2}{V_r} \left[U_0 - C_c \sqrt{\frac{2}{\rho_a}} A(q) \sqrt{P_A(t)} - \mathcal{E}\dot{q}(t) \right] \quad (3)$$

where the total exit area of the aperture can be written as

$$A = 2 \int_0^{L_b} \sqrt{\phi^2(s)q^2 + b^2} ds + W_b \sqrt{\phi^2(L_b)q^2 + b^2} \quad (4)$$

Here, $q(t)$ is a generalized temporal coordinate representing the beam's tip deflection, ζ is the mechanical damping ratio, ω is the first modal frequency of the beam, Θ is the electromechanical coupling, C_p is the piezoelectric capacitance, ρ_a is air density, c is the speed of sound, V_r is the volume of the chamber, C_c is a flow contraction coefficient, and \mathcal{E} represents the projection of the pressure forces on the beam's first modal response. Furthermore, $\phi(s)$ is the beam's first modal shape, and W_b and L_b represent its width and length, respectively. A detailed description of these constants as functions of the beam and flow properties is available in Appendix 1.

The derived model assumes that a constant flow rate of air is supplied by a high-impedance source through a very small aperture. The chamber is assumed to be long enough to permit the flow to fully develop such that the inlet and outlet flows do not interact with each other directly. Furthermore, acoustic resonances in the pipe are neglected under the assumption that such resonances are only excited within a small bandwidth of frequencies where one of the beams' modal frequencies matches one of the pipes' acoustic resonance frequencies. The preceding model also imposes several assumptions on the fluid motion and properties. The fluid is assumed to be inviscid because air has a very low viscosity at normal temperatures. The flow through the aperture is assumed to be two-dimensional, irrotational, laminar, and steady following the studies of Tarnopolsky et al. (2000, 2001) and Ricot et al. (2005) on music-playing harmonicas.

This article utilizes equations (1) to (4) to investigate the role that the design parameters play in the transduction of this MPG. Specifically, it analyzes the influence of the beam's dimensions, chamber volume, electric load, and aperture size on the cut-in wind speed and output power of the device. To achieve this objective, section "Cut-in wind speed" implements a stability analysis to construct the mathematical conditions necessary

for the onset of beam's limit-cycle oscillations (Hopf bifurcation curves). Subsequently, these conditions are utilized in conjunction with a Newton–Raphson optimization scheme to obtain the design parameters that minimize the cut-in wind speed of the device. Section "Output power" presents a numerical investigation of the influence of the design parameters on the output power and generates design charts to assist in choosing the optimal parameters for a known average wind speed. Section "Case study" provides several qualitative verifications of the theoretical trends through an experimental case study. Section "Power coefficient" discusses the power coefficient of the harvester, and, finally, section "Conclusion" summarizes the important findings.

Cut-in wind speed

The onset of the limit-cycle oscillations necessary for energy generation (cut-in wind speed) is governed by a threshold combination of the flow and design parameters known as the *Hopf bifurcation* point. Beyond that threshold, the nonlinear pressure forces overcome the intrinsic damping in the system, and the beam undergoes limit-cycle oscillations around a static equilibrium position. The combination of the design parameters at which the cut-in wind speed occurs can be obtained by analyzing the stability of the equilibria of equations (1) to (3). These can be found by setting the time derivatives in the aforementioned equations equal to zero to obtain the following algebraic equations

$$q_s A^2 - \frac{\mathcal{E}\rho_a}{2\omega^2 C_c^2} = 0, \quad P_s = \frac{\omega^2}{\mathcal{E}} q_s, \quad V_s = 0 \quad (5)$$

where q_s , P_s , and V_s are used to represent the static deflection, static pressure, and direct current (DC) output voltage, respectively, for a given input flow rate, U_0 . It is worth mentioning that since the area of the aperture is a nonlinear function of q as given in equation (4), the static equations can only be solved numerically.

The stability of the resulting equilibria is assessed by expanding the phase space to include \dot{q} and constructing the Jacobian of the system dynamics. For the fourth-order system considered, setting the determinant of the Jacobian matrix equal to zero yields the following fourth-order characteristic equation that can be used to determine the eigenvalues of the system response

$$\lambda^4 + \omega(\alpha_c + \alpha_r + 2\zeta)\lambda^3 + \omega^2[1 + z_r + \alpha_c\alpha_r + \kappa^2 + 2\zeta(\alpha_r + \alpha_c)]\lambda^2 + \omega^3[z_r + \alpha_c + 2\zeta\alpha_r\alpha_c + \alpha_r(1 + 2\eta + \kappa^2)]\lambda + \omega^4\alpha_c\alpha_r(1 + \eta) = 0 \quad (6)$$

where the following nondimensional constants have been introduced: $\alpha_c = 1/(RC_p\omega)$ is the ratio between the harvesting circuit time constant and the first modal frequency of the beam, $\alpha_r = c^2 C_c^2 A^2 / (V_r U_0 \omega)$ is the ratio between the time constant of the pressure dynamics

and the natural frequency of the beam, $\kappa = \Theta^2 / (\omega^2 C_p)$ is a nondimensional electromechanical coupling constant, $z_r = \rho c^2 \mathcal{E}^2 / (V_r \omega^2)$ denotes the ratio between the acoustic impedance of the chamber and the mechanical impedance of the beam, and finally $\eta = q_s (dA/dq_s) / A$ is a nondimensional constant that lumps the effect of the aperture shape and area on the response.

From a mathematical perspective, the cut-in wind speed represents a Hopf bifurcation point at which one or more pairs of complex conjugate eigenvalues associated with the Jacobian matrix have a nonzero velocity crossing of the imaginary axis. This pair of eigenvalues takes the form $\lambda_{1,2} = \pm i \varpi$, where ϖ represents the frequency of the born limit cycle just beyond the cut-in speed. With this knowledge, the critical wind speed can be found by substituting $\lambda = \pm i \varpi$ into equation (6), separating the real and imaginary parts, then setting each part equal to zero separately. This yields

$$\Omega^2 = \frac{\alpha_c(1+z_r+2\zeta\alpha_r) + \alpha_r(1+2\eta+\kappa^2)}{\alpha_c + \alpha_r + 2\zeta} \quad (7a)$$

$$\Omega^4 - \Omega^2(1+z_r+\alpha_c\alpha_r+2\zeta(\alpha_c+\alpha_r+\kappa^2)) + \alpha_c\alpha_r(1+2\eta) = 0 \quad (7b)$$

where $\Omega = \varpi/\omega$ is the frequency ratio. Equations (7a) and (7b) can now be solved simultaneously for the critical flow rate U_{cr} embedded within α_r and the associated limit-cycle oscillation frequency embedded within Ω . Through further analysis, not shown here, it can be shown that the pair of eigenvalues $\lambda_{1,2}$ has a traversal (nonzero velocity) crossing of the imaginary axis. With these conditions satisfied, one can correctly surmise that a limit cycle with period $2\pi/\varpi$ is born as a result of a Hopf bifurcation at (P_s, q_s, U_{cr}) when equations (7a) and (7b) are simultaneously satisfied. It is worth noting,

however, that not every set of design parameters can yield a real value of the critical flow rate. In such a scenario, the beam bends to a static position without oscillating around it regardless of the input flow rate.

Figure 2 illustrates bifurcation diagrams of the static tip deflection and the static pressure for the system parameters given in Table 1. It is evident that the static position loses stability at $U_0 = U_{cr}$, after which the stable static solution gives way to limit-cycle oscillations.

Without a numerical study, equations (7a) and (7b) are too involved to provide a good understanding of the influence of the design parameters on the cut-in wind speed. However, for some special cases, it is possible to gain some physical insight by carefully inspecting those equations. In what follows, we treat two particular cases:

Short-circuit condition

When R approaches zero, α_c approaches infinity, and the harvester reduces to an oscillating beam in an aerodynamic flow, similar to a harmonica reed. Under such assumption, the frequency of the beam oscillations just beyond the cut-in wind speed can be expressed as

$$\Omega^2 = 1 + z_r + 2\alpha_r\zeta, \quad \varpi^2 = \omega^2(1 + z_r + 2\alpha_r\zeta) \quad (8)$$

Equation (8) reveals that the beam oscillation frequency is always greater than the first modal frequency due to the influence of the trapped air in the chamber, which acts as a stiffening spring. The increase in the frequency is mostly pronounced for small chamber volumes because the impedance ratio z_r and the time constant ratio α_r are inversely proportional to V_r . The associated critical flow rate, which is inversely

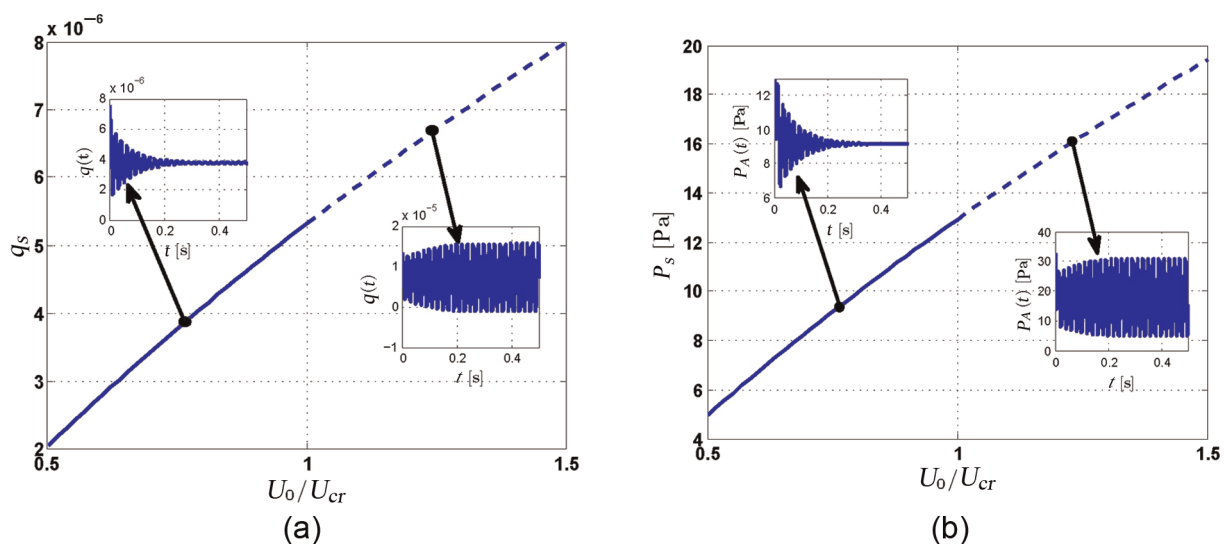


Figure 2. Stability and bifurcations of (a) the static deflection, q_s , and (b) the static pressure, P_s . Dashed lines represent unstable static solutions.

Table 1. Geometric and material properties of the Geometric and material properties of the harvester.

	Steel
Properties/beam material	
Modulus of elasticity, Y^b (GPa)	190
Density, ρ^b (kg/m ³)	7900
Length, L_b (mm)	59
Width, W_b (mm)	17
Thickness, t_b (mm)	0.127
Gap width, b (mm)	0.2
Piezoelectric layer	
Density, ρ^p (kg/m ³)	7850
Length, L_p (mm)	7.95
Width, W_p (mm)	13
Modulus of elasticity, Y^p (GPa)	66
Thickness, t_p (mm)	0.102
Electromechanical coupling, d_{31} (pm/V)	-190
Permittivity, ϵ_{33} (nF/m)	15.93
Other	
Air density, ρ_a (kg/m ³)	1.2
Speed of sound, c (m/s)	340
Contraction coefficient, C_c	0.63
Chamber volume, V_r (L)	2.4
Electrical load, R (k Ω)	50

proportional to α_r , can be obtained by substituting equation (8) into equation (7b) and solving for α_r . This yields

$$\alpha_r = \frac{2\eta - z_r - 4\zeta^2 + \sqrt{(2\eta - z_r - 4\zeta^2)^2 - 16(1 + \eta)\zeta^2}}{4\zeta} \tag{9}$$

Perhaps, the most important conclusion resulting from equation (9) lies in the fact that α_r and, hence, U_{cr} can only admit real values when $(2\eta - z_r - 4\zeta^2)^2 \geq 16(1 + \eta)\zeta^2$ further emphasizing that a critical inflow rate that sets the beam into limit-cycle oscillations does not always exist. Equation (9) also highlights the critical effect of the static deflection as well as the shape and size of the aperture area embedded within η on the critical inflow rate. Specifically, the critical inflow rate appears to be inversely proportional to η . As expected, it can also be deduced that the critical inflow rate is directly proportional to the mechanical damping ratio.

Open-circuit condition

When R approaches infinity, α_c approaches zero, and the frequency of beam oscillations just beyond the cut-in wind speed becomes

$$\Omega^2 = \frac{1 + 2\eta + \kappa^2}{1 + 2\zeta/\alpha_r}, \quad \omega^2 = \omega^2 \left(\frac{1 + 2\eta + \kappa^2}{1 + 2\zeta/\alpha_r} \right) \tag{10}$$

Since, in general, $\zeta/\alpha_r \ll 1$, the oscillation frequency is again greater than the modal frequency of

the beam. The shift is due to the static deflection of the beam within η and the coupling coefficient, κ^2 . When η is set to zero, the oscillation frequency reduces to $\omega = \omega\sqrt{1 + \kappa^2}$, which represents the antiresonant frequency of a piezoelectric harvester.

Substituting equation (10) back into equation (7b), we obtain the following expression for the critical α_r

$$\alpha_r = \frac{2\eta - z_r - 4\zeta^2 + \sqrt{(2\eta - z_r - 4\zeta^2)^2 - 16(1 + \eta)\zeta^2 - 16\zeta^2\kappa^2}}{4\zeta} \tag{11}$$

which is similar to equation (9) with the additional term, $-16\zeta^2\kappa^2$, under the square root. This term is usually small indicating a slight increase in the critical inflow rate as compared to the short-circuit scenario.

In what follows, we use equations (7a) and (7b) to carry a numerical investigation to study the influence of the design parameters, namely, the chamber volume, beam dimensions, aperture width, and electric load on the critical inflow rate with the goal of minimizing the cut-in wind speed of the MPG. Unless otherwise indicated, the simulations will be presented for the parameters listed in Table 1.

Chamber volume

In music-playing harmonicas, the volume of the air chamber has a significant influence on the magnitude of the static pressure necessary to activate its reeds. Since, for the generator under consideration, the magnitude of the static pressure exerted on the surface of the cantilever is proportional to the square of the wind speed, it is expected that the chamber volume plays an important role in minimizing the cut-in wind speed of the device. Figure 3 shows the variation of the critical inflow rate, U_{cr} , with the chamber volume, V_r , for different beam lengths, L_b . The results clearly illustrate

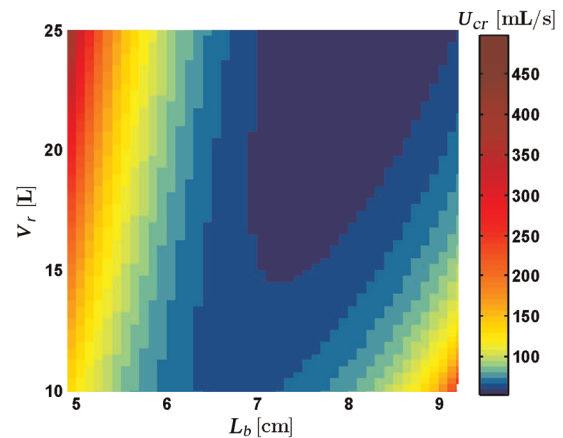


Figure 3. Variation of the critical inflow rate, U_{cr} , with the chamber volume, V_r , and the beam length, L_b .

the presence of an optimal chamber volume for each beam length at which U_{cr} can be minimized. Designing the MPG with a chamber volume that is relatively far from the optimal one can dramatically increase its cut-in wind speed.

Using a Newton–Raphson optimization scheme, we study the variation of the optimal chamber volume and the associated U_{cr} with the beam's dimensions as depicted in Figure 4(a) and (b). To minimize the calculation time, the numerical subroutine searching for the optimal volume was restricted to a maximum volume of 25 L. Any combinations of (L_b, t_b) that yield an optimal volume larger than 25 L were automatically discarded. Figure 4(a) and (b) illustrates that the optimal volume decreases as the beam thickness is increased and increases with its length, which leads to the conclusion

that the optimal volume is inversely proportional to the square of the beam's first modal frequency as shown in Figure 5(a). This result implies that the optimality of the design does not impede its scalability. Specifically, since the optimal chamber volume decreases as the first modal frequency increases, and the first modal frequency generally increases as the size of the beam decreases, it is safe to conclude that the optimal volume of the chamber will be smaller for smaller beams.

Figure 5(a) also demonstrates that the optimal volume is dependent on the beam's modal frequency but not on the actual dimensions. In another words, beams with equal frequencies have the same optimal volume regardless of their actual geometric or material properties. On the other hand, the critical inflow rate corresponding to the optimal volume is dependent not only

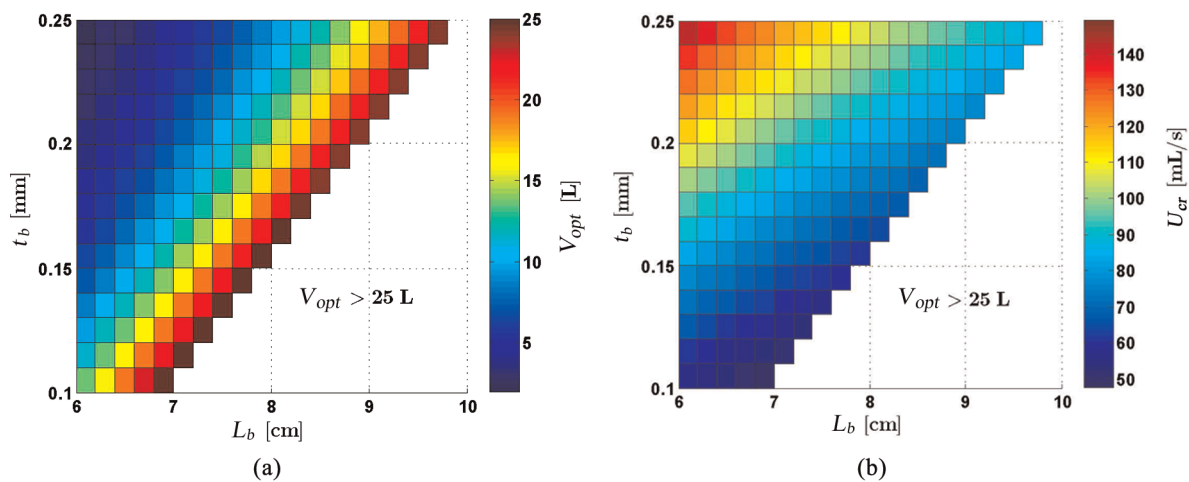


Figure 4. (a) Optimal chamber volume, V_r , and (b) associated critical inflow rate, U_{cr} , as a function of beam's length, L_b , and thickness, t_b .

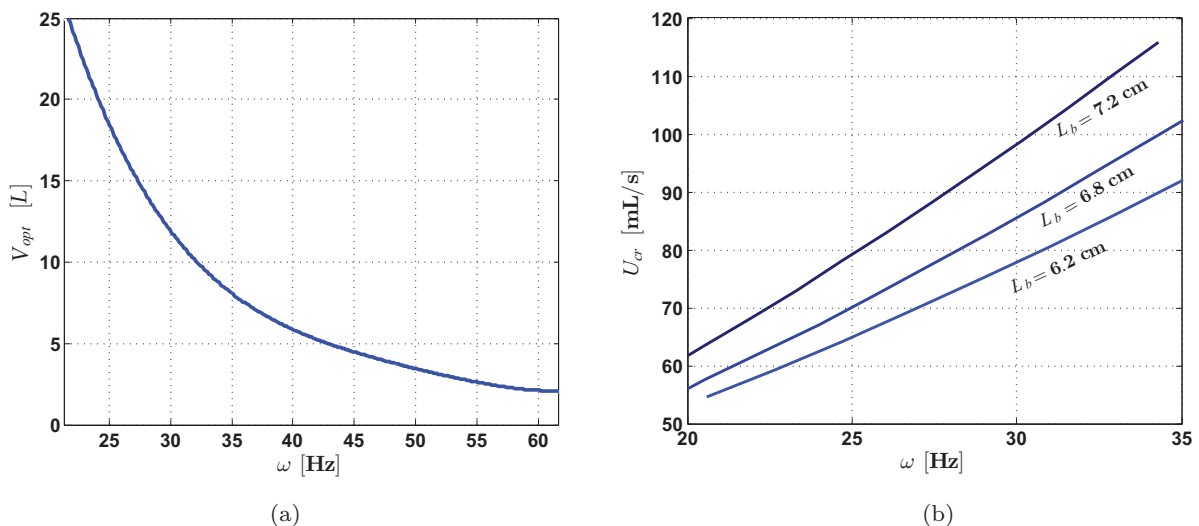


Figure 5. (a) Optimal chamber volume, V_r , as a function of beam's first modal frequency and (b) the critical inflow rate, U_{cr} , as a function of beam's first modal frequency and for different beam lengths. Frequency is changed by changing the thickness.

on the frequency but also on the relative dimensions of the beam as shown in Figure 5(b). For a given frequency, the critical inflow rate increases with the beam's length, while, for a given length, the critical inflow rate increases with the frequency that increases as the thickness is increased. From a design perspective, these results can aid in choosing the proper beam dimensions in conjunction with the optimal volume such that the design meets the requirement on the critical wind speed.

Aperture width

In addition to the chamber's volume, the aperture size, area, and gap width, b , play a critical role in minimizing the cut-in wind speed of the device. This is evident by the analytical expressions obtained for the critical flow rate in sections "Short-circuit condition" and "Open-circuit condition." To further elucidate this role, the gap width is varied between 0.15 and 0.3 mm for the same beam, and the cut-in wind speed is calculated for different chamber volumes as shown in Figure 6. Which shows that the cut-in wind speed that is proportional to U_{cr} decreases with the gap width for any chamber volume. As such, at the MPG's optimal volume, the gap width should be minimized. Realizing smaller gaps, however, can be limited by manufacturing processes, especially at the macroscale. If the device was to be manufactured at the microscale, small gaps with a submicron resolution can be easily realized using a simple etching process.

Electric load

As the electric load is varied, the electric damping in the system changes influencing the critical cut-in wind speed necessary for the onset of beam's oscillations. While this influence is not very dramatic, it can be clearly observed in Figure 7. As the electric load

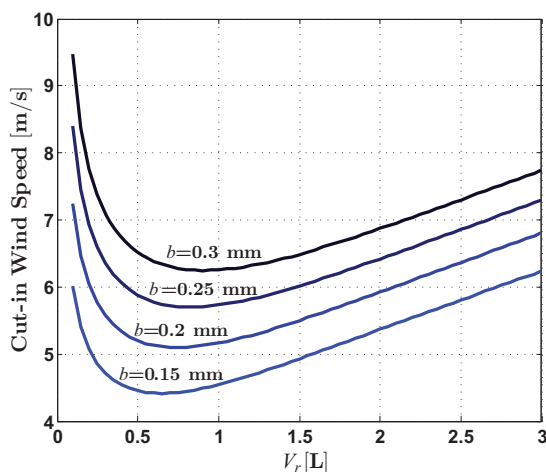


Figure 6. Cut-in wind speed curves as a function of the chamber's volume for different gap widths.

increases from short-circuit conditions, the critical inflow rate increases and exhibits a maximum at a certain load resistance ($R \approx 225 \text{ k}\Omega$) where the electric damping is also maximized. In agreement with the discussion deduced from equations (9) and (11), the open-circuit critical inflow rate is larger than that associated with the short circuit.

For a traditional linear piezoelectric vibratory energy harvester, the optimal load resistance that maximizes the output power can be approximated via impedance matching between the mechanical element and the electric circuit. This yields the expression $R_{opt} = 1/(C_p \omega)$, which, for the numerical values used in this study, gives $R_{opt} \approx 230 \text{ k}\Omega$. Quite interestingly, this value is very close to the load at which the critical inflow rate is maximized.

Output power

The process of minimizing the cut-in wind speed of the device does not necessarily guarantee an increase in its output power. For instance, consider Figure 8(b), which illustrates variation of the steady-state amplitude of the output voltage with the inflow rate calculated at the optimal volume for different beam lengths. If the average inflow rate at the location where the harvester is designed to operate is greater than $U_0 = 80 \text{ mL/s}$, the shorter beam that yields the highest cut-in wind speed will provide maximum output voltage. This can be attributed to the fact that minimizing the cut-in wind speed does not necessarily yield an optimal strain rate in the piezoelectric patch, which is essential for maximizing the output power.

Optimal design charts

Figure 8 shows the effect of several beam design parameters on the steady-state voltage. A steel beam is

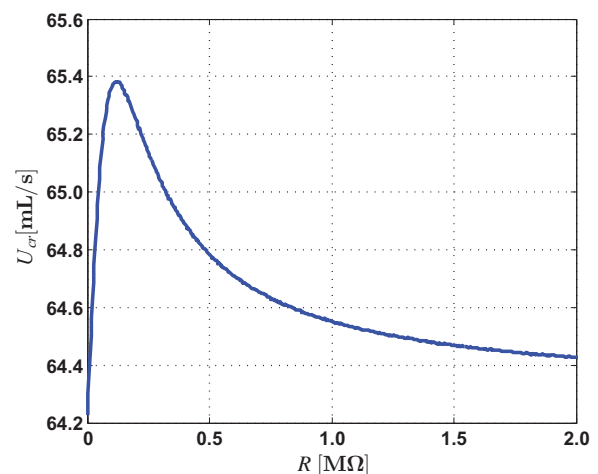


Figure 7. Variation of the critical inflow rate, U_{cr} , with the load resistance.

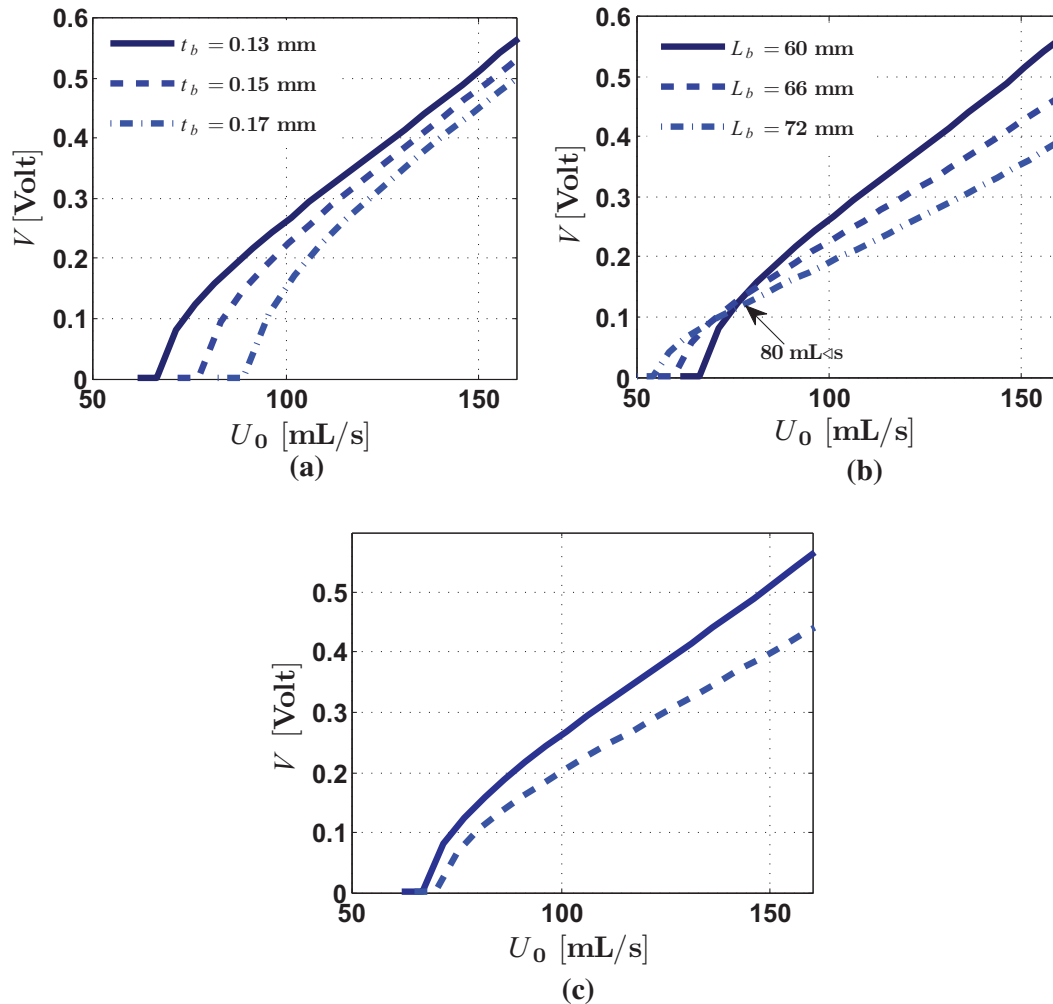


Figure 8. Bifurcation diagram comparison: (a) $L_b = 60$ mm; (b) $t_b = 0.13$ mm; and (c) solid ($L_b = 60$ mm, $t_b = 0.13$ mm) and dashed ($L_b = 66$ mm, $t_b = 0.15$ mm).

considered, and six design specifications are studied: ($L_b = 60$ mm, $t_b = 0.13$ mm), ($L_b = 60$ mm, $t_b = 0.15$ mm), ($L_b = 60$ mm, $t_b = 0.17$ mm), ($L_b = 66$ mm, $t_b = 0.13$ mm), ($L_b = 72$ mm, $t_b = 0.13$ mm), and ($L_b = 66$ mm, $t_b = 0.15$ mm). The amplitude of the voltage response is then calculated for a resistance of $R = 50$ k Ω and using the optimal volume for all configurations, which is found to be 8.5L, 6.5L, 5L, 14L, 22L, and 10.5L, respectively. The resistance chosen was fixed at a nonoptimal value, which is far away from the optimal resistance corresponding to any of these designs such that the effect of the beam dimensions can be separately addressed. Figure 8(a) shows the voltage diagram for the reference beam, first case, compared to the thicker beams, second and third cases. The results suggest that while maintaining an optimal volume, increasing the beam thickness shifts the whole bifurcation diagram toward higher critical flow rates. In other words, a thinner beam will produce a larger output voltage than a thicker one. When the thickness of the beam increases, the frequency of beam's oscillation increases, while the

associated amplitude decreases for the same inflow rate. The result is that the decrease in the amplitude overcomes the increase in the frequency, thereby reducing the strain rate and hence the output voltage. One has to bear in mind, however, that reducing the thickness of the beam significantly does not necessarily yield larger power levels. In such limiting cases, the piezoelectric layer can become stiffer than the beam, and hence, very little strain will be produced in the piezoelectric patch even when the beam undergoes large-amplitude oscillations.

A comparison between the steady-state voltage curves of the reference beam and a longer beam, third and fourth cases, is shown in Figure 8(b). As explained previously in Figure 4(b), for a given thickness, increasing the length of the beam decreases the cut-in wind speed. Here, it is shown that, it also has the adverse influence of decreasing the slope of the voltage-inflow rate curves. As a result, the curves intersect at a certain inflow rate. This can cause a longer beam, which has a lower cut-in wind speed to produce lower voltages at

higher wind speeds. Again, the intersection of the voltage curves can be attributed to a critical balance between the strain in the piezoelectric patch and the frequency of oscillations. This clearly illustrates that prior knowledge of the average wind speed at the location where the MPG is designed to operate is necessary in order to select the optimal design parameters. Figure 8(c) demonstrates how changing both the beam's length and thickness affect the bifurcation diagrams.

As seen throughout the preceding analysis, there are many parameters that can be optimized to enhance the MPG's output power. In an effort to provide a quick methodology for the selection of these design parameters, we generate in Figure 9 design charts that can be used to maximize the output voltage of the MPG subjected to user's constraints. Prior to using these charts, a designer should have an idea about the average wind speed at the location where the MPG is designed to operate and the space limitations that can

constrain the maximum size of the MPG represented in its chamber volume V_r . For the sake of illustration, the output voltage of the MPG is calculated at two different locations having an average wind speeds of 4 and 7 m/s, as shown in Figure 9(a) and (b). The background color, filled contours, shows the steady-state amplitude of the output voltage, V , that is calculated at the optimal V_r associated with each combination of (L_b, t_b) and $R = 50 \text{ k}\Omega$. It is worth noting that since V_r is kept constant at 25 L for beams that require larger optimal volumes, these results are suboptimal for beam dimensions that require a larger optimal volume. The solid-lined contours represent the bifurcation inflow rate, U_{cr} , required to activate the MPG. The dash-lined contours display the associated optimal volume, V_r .

The charts indicate the presence of two main regions in the (t_b, L_b, V_r) space that maximize the output voltage for a given average wind speed. These large-amplitude voltage regions shift to the left along the thickness axis for the higher average wind speeds. The drop appearing in the output voltage between these two regions occurs for volumes exceeding 25 L and could be a result of the volume constraint placed on the optimization algorithm. By comparing Figure 9(a) and (b), it can also be clearly seen that a shorter beam provides a higher voltage at the higher wind speeds.

Electric load

Earlier in section "Electric load," we studied the influence of the electric load on the cut-in wind speed and illustrated that, while present, the influence is very small. In this section, we investigate the influence of the electric load on the output power. As mentioned previously, based on impedance matching conditions for linear systems, the optimal electric load that maximizes the output power is constant and can be approximated as $R_{opt} = 1/(C_p \omega)$, where ω is the first modal frequency of the beam. For the nonlinear system at hand, where the frequency of the resulting limit-cycle oscillations is not constant but rather depends on the inflow rate as shown in Figure 10(a), the optimal electric load changes with the inflow rate as shown in Figure 10(b). These variations, however, are not very significant because the frequency of limit-cycle oscillations, denoted here as ω_m , is not very sensitive to variations in U_0 . As such, close to the critical inflow rate, it is sufficient to use an optimal load based on linear impedance matching because *near* optimal power can be harnessed as shown in Figure 10(c). However, as the flow rate increases significantly from its critical value, nonlinear impedance matching shows 5% more output power than the linear case at $U_0 = 2U_{cr}$.

As the design parameters are varied, the optimal electric load varies significantly. Figure 11 shows the variations of the optimal load calculated at $U_0 = 1.2U_{cr}$

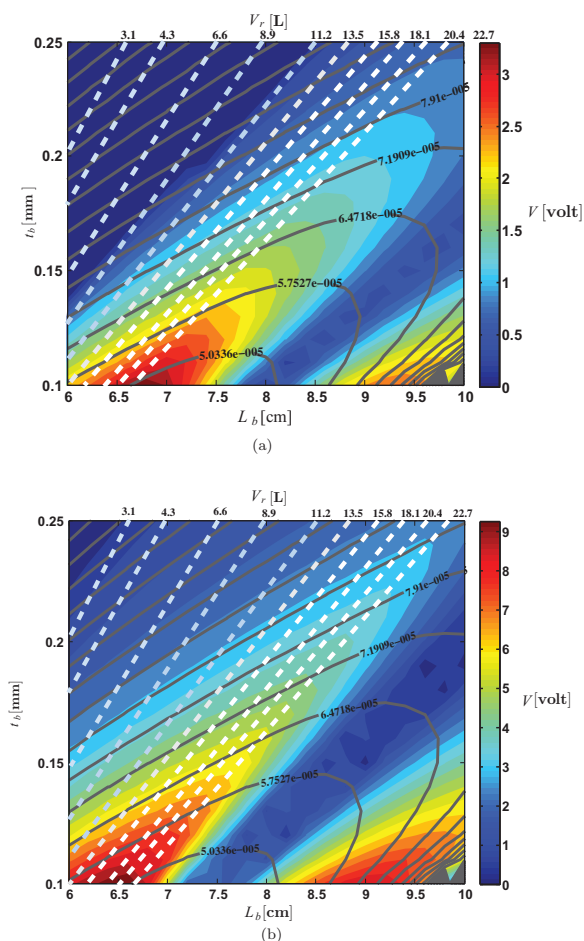


Figure 9. Design charts obtained at different average wind speeds: (a) 4 m/s and (b) 7 m/s. The filled contours represent the amplitude of the output voltage, V , solid-lined contours represent the bifurcation inflow rate, U_{cr} , required to activate the MPG in millimeter, and the dash-lined contours display the associated optimal volume, V_r .

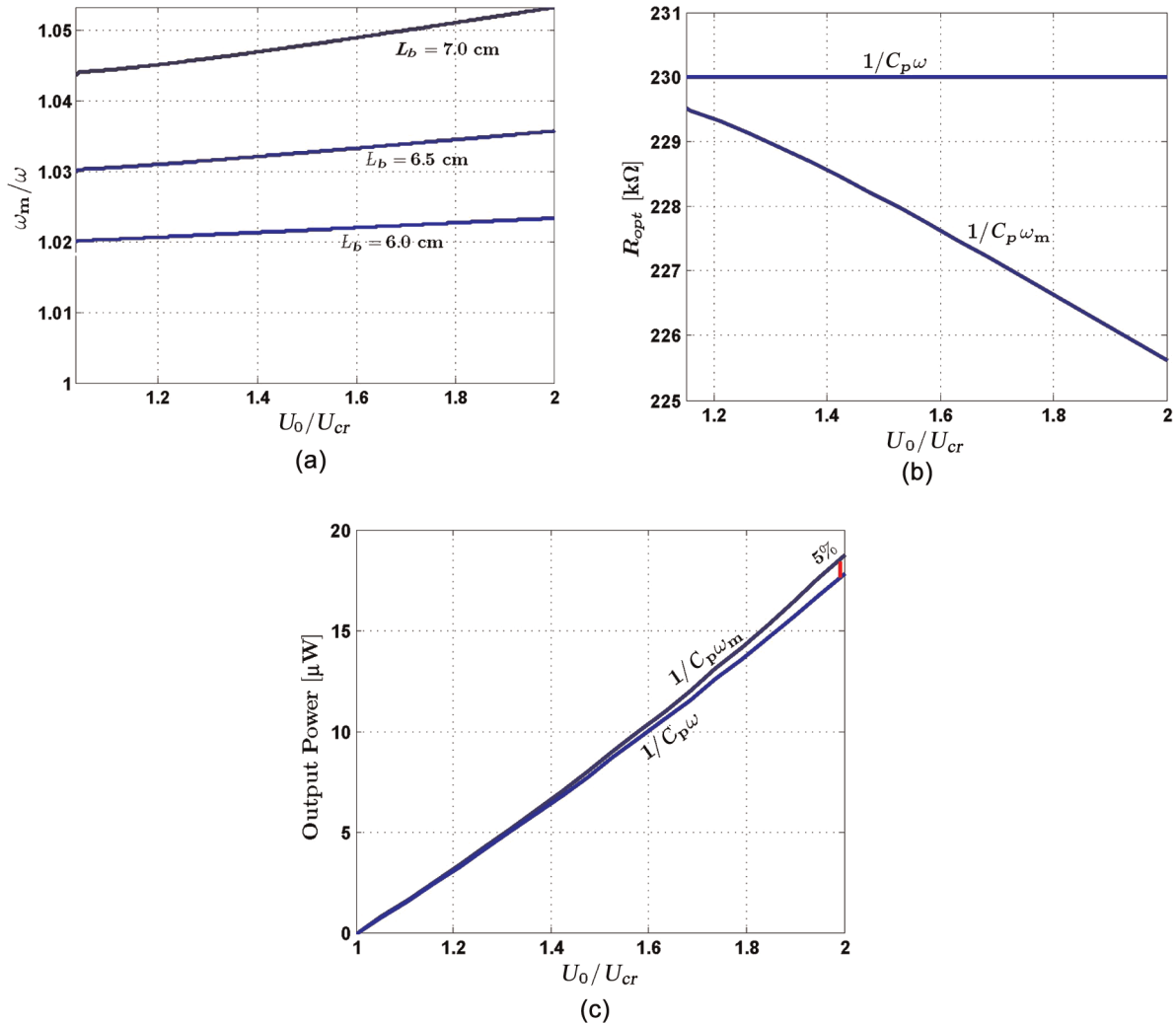


Figure 10. (a) Response frequency, ω_m , as a function of inflow rate ratio for different beam lengths, (b) optimal load as a function of the inflow rate, and (c) the output power associated with the optimal load.

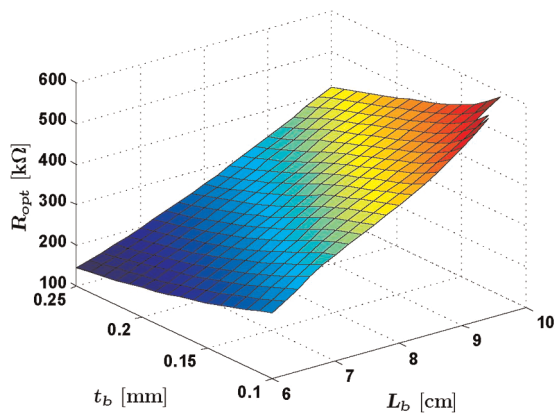


Figure 11. Optimal load as a function of the beam's length, L_b , and thickness, t_b , calculated at $U_0 = 1.2U_{cr}$.

for different beam lengths and thicknesses. The figure demonstrates that the optimal load is inversely proportional to the beam's first modal frequency.

Case study

In this section, we verify some of the theoretical trends experimentally using the setup shown in Figure 12. As a case study, we consider the objective of developing an MPG that is capable of producing $50 \mu\text{W}$ of average power at an average wind speed of 7.5 m/s . This can represent powering a sensor interface chip for health monitoring in Charleston, South Carolina (Baerta et al., 2006). The design involves the selection of materials and dimensions based on realistic fabrication constraints and performance requirements. An aluminum unimorph harvester is considered in this case. The geometric, material, and the electromechanical parameters of the beam are given in Table 2. First, the optimal chamber volume that minimizes the cut-in wind speed is investigated. The length of the polyvinyl chloride (PVC) tube and, hence, its volume are varied. Air is supplied from a high-impedance source via a small aperture at one end of the chamber. The average

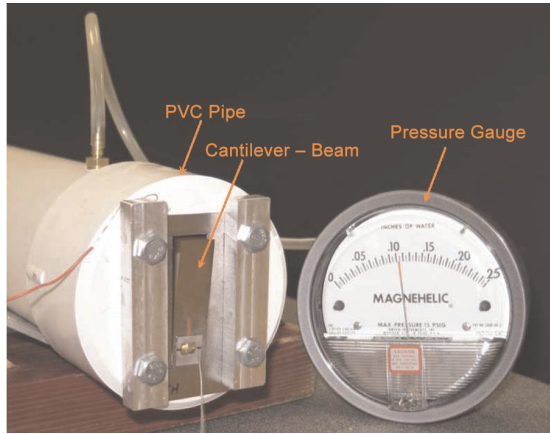


Figure 12. Experimental setup.

Table 2. Geometric and material properties of the beam and piezoelectric layer used in the experiments.

	Aluminum
Properties/beam material	
Modulus of elasticity, Y^b (GPa)	70
Density, ρ^b (kg/m^3)	2700
Length, L_b (mm)	58
Width, W_b (mm)	16.25
Thickness, t_b (mm)	0.38
Piezoelectric layer	
Density, ρ^p (kg/m^3)	7850
Length, L_p (mm)	13.5
Width, W_p (mm)	12.7
Modulus of elasticity, Y^p (GPa)	66
Thickness, t_p (mm)	0.127
Electromechanical coupling, d_{31} (pm/V)	-190
Permittivity, ϵ_{33} (nF/m)	15.93
Other	
Air density, ρ_a (kg/m^3)	1.2
Speed of sound, c (m/s)	340
Contraction coefficient, C_c	0.63

pressure is then measured using a pressure gage and related using the steady Bernoulli’s equation to an equivalent velocity, which, when supplied at the input assuming a fully developed flow, generates the same pressure condition in the chamber. When the volume is increased from 0.93 to 2.3 and 2.8 L, the threshold pressure was measured at 91 Pa (12.2 m/s), 52 Pa (9.2 m/s), and 76 Pa (11.4 m/s), respectively, as shown in Figure 13(a). None of these designs have a cut-in wind speed below 7.5 m/s. Consequently, as concluded from the theoretical analysis, we reduce the gap width as shown in Figure 13(b). Reducing the gap width to $b=0.05$ mm, yields a threshold pressure significantly less than 34 Pa (7.5 m/s).

The steady-state output voltage of the MPG is investigated experimentally, Figure 14(a), for $V_r=2.3$ L and $V_r=2.8$ L. Figure 14(a) demonstrates how choosing a nonoptimal volume increases the cut-in speed significantly by shifting the bifurcation diagram toward higher values.

Next, we investigate the MPG’s response and the range of achievable output power. Figure 14(b) shows the variation of the experimental average output power with the input pressure for a 120-k Ω load. It can be seen that the output power at 7.5 m/s, 34 Pa, is still less than the desired power of 50 μW . To increase the power, one can reduce the gap even further or change the volume to match the exact optimal value. However, we elect to optimize the electric load, as a nonoptimal 120-k Ω load was used in the previous experiments.

Based on the theoretical model, the optimal load was calculated at $R_{opt} = \frac{1}{C_p \omega} \approx 62$ k Ω . Experimentally, the electric load is varied, and the output power is measured at a wind speed of 7.5 m/s as shown in Figure 15. A maximum power of 55 μW is measured near $R \approx 70$ k Ω , showing acceptable agreement between the

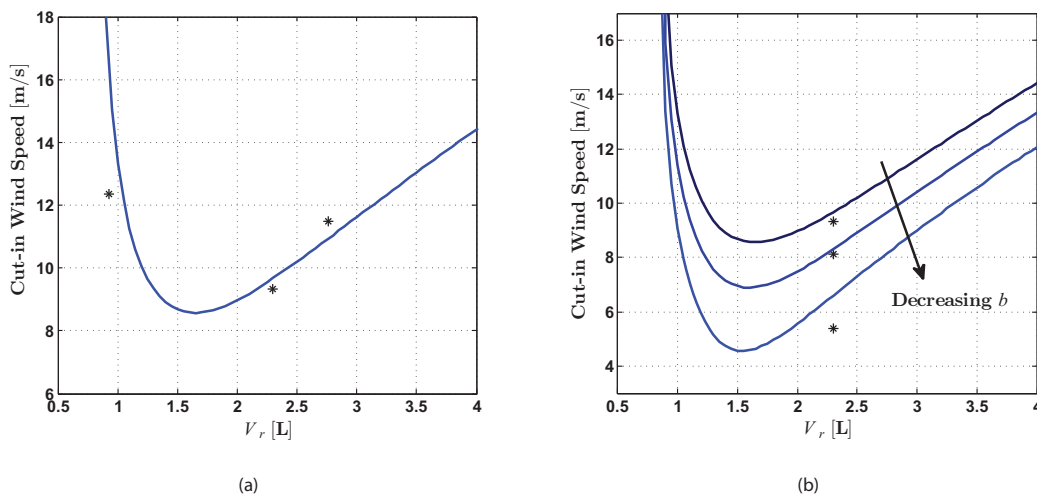


Figure 13. (a) Cut-in wind speed as a function of chamber volume, V_r , for a gap width $b=0.15$ mm, and (b) cut-in wind speed as a function of chamber volume, V_r , and gap widths, $b=0.05$ mm, 0.1 mm, and 0.15 mm. The results are obtained for $R=120$ k Ω : solid lines represent theoretical data and asterisks represent experimental data.

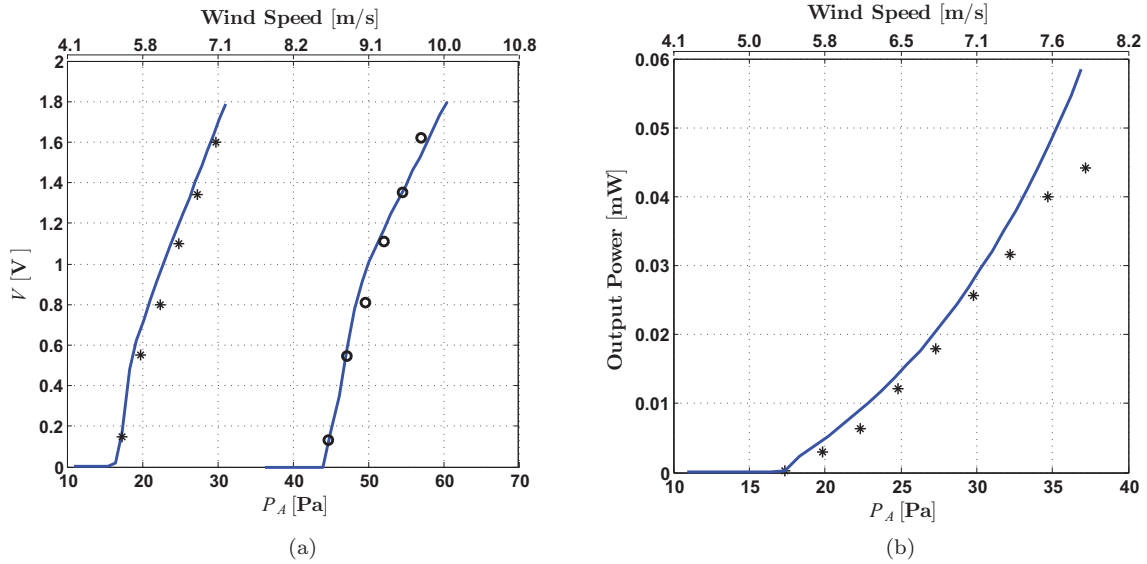


Figure 14. (a) Variation of the output voltage with the input pressure for different chamber volumes, V_r : 2.3 L (asterisks) and 2.8 L (circles), and (b) variation of the output power with the input pressure for $V_r = 2.3$ L. The results are obtained for $b = 0.05$ mm and $R = 120$ k Ω : solid lines represent theoretical data, and asterisks

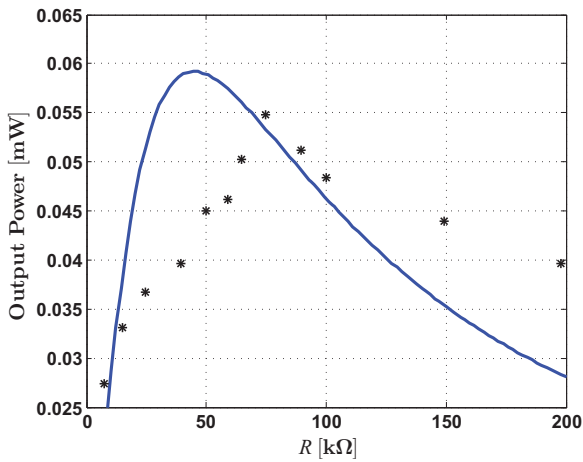


Figure 15. Variation of the output power with the electric load. The results are obtained at 7.5 m/s wind speed for $b = 0.05$ mm and $V_r = 2.3$ L: solid line represent theoretical data, and asterisks represent experimental data.

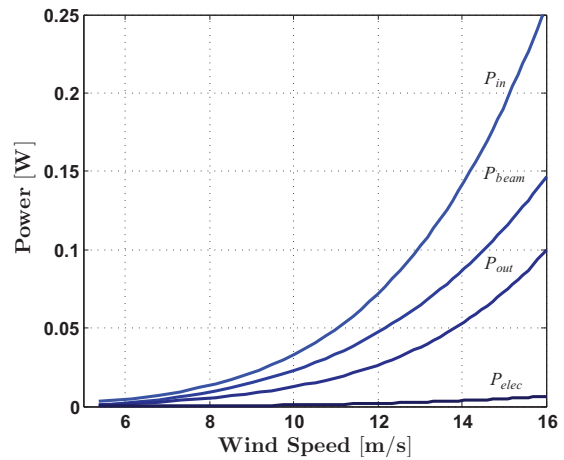


Figure 16. Variation of the power with the wind speed.

theory and experiments. At this electric load, the device is shown to meet the performance criterion set initially.

Power coefficient

To evaluate the overall performance of the harvester, it is useful to determine the efficiency by which energy is being extracted from the flow. The power of the input flow is characterized by two main variables, pressure and flow rate, whose product gives the input power, $P_{in} = P_A(t)U_0$. The total energy captured by the beam, which includes the kinetic energy, potential energy, and energy dissipation due to the mechanical and electrical damping, can be determined via

$$E_{beam} = W_b \int_0^{L_b} P_A(t)w(s, t) ds \tag{12}$$

where $w(s, t)$ is the spatiotemporal deflection of the cantilever beam, which can be replaced by $\phi(s)q(t)$. Taking the time derivative of E_{beam} gives the following expression for total power accessed by the beam

$$P_{beam} = \mathcal{E}[\dot{P}_A(t)q(t) + P_A(t)\dot{q}(t)] \tag{13}$$

The power of the flow exiting the aperture is determined by $P_{out} = \frac{1}{2}\rho_a A(t)V_{out}^3$, where $V_{out} = U(t)/A(t)$. Finally, the electric power is given by $P_{elec} = V^2(t)/R$.

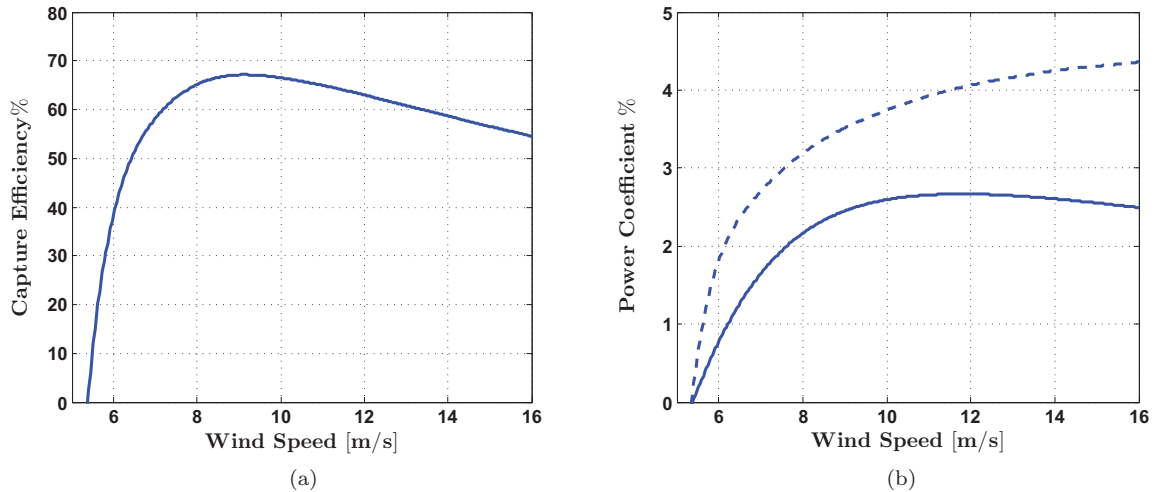


Figure 17. (a) Variation of the capture efficiency of the beam with the wind speed and (b) power coefficient: electrical to mechanical power (dashed line) and electrical to inflow power (solid line).

Figure 16 shows the root mean square (RMS) value of the inflow power, outflow power, power extracted by the beam, and the electric power as a function of wind speed. The capture efficiency, which shows the percentage of the power in the flow accessed by the beam, is also shown in Figure 17(a), demonstrating a high value of 67% at around 8.5 m/s. The power coefficient of the harvester, which characterizes the conversion efficiency from mechanical to electric power and the overall efficiency from inflow power to electric power at various wind speeds, is shown in Figure 17(b). Figure 17(b) demonstrates that the power coefficient is high in the midwind speed range and could reach a maximum value of 2.7% at a wind speed of 11.5 m/s.

Conclusion

To optimize the performance of an aeroelastic MPG, this effort systematically analyzed the influence of the design parameters on its cut-in wind speed and the resulting output power. First, the Hopf bifurcation condition is derived and utilized through numerical simulations to study the effect of the chamber volume and aperture width on the cut-in wind speed of the device for different beam dimensions. The results show that for a given beam, there exists an optimal chamber volume that minimizes the cut-in wind speed. This optimal volume is inversely proportional to the square of the beam's first modal frequency regardless of its specific dimensions or material properties. On the other hand, the cut-in wind speed corresponding to the optimal volume is shown to depend on the relative dimensions of the beam. The results also indicate that the cut-in wind speed can be decreased significantly as the aperture's width is decreased. Second, the steady-state voltage-inflow rate curves are compared at the optimal volume for beams with different sizes. It is shown that

minimizing the cut-in wind speed does not always correspond to an increase in the output power. As such, design charts are constructed to identify the design parameters that yield the optimal performance of the generator for a known average wind speed. To maximize the flow of energy from the vibrating structure to the electric load, the optimal load resistance that maximizes the output power is also investigated. It is illustrated that the optimal load does not vary considerably with the inflow rate and that it can be well approximated using linear impedance matching conditions. Finally, an experimental design case of a 50- μ W MPG is conducted to verify some of the theoretical trends.

Acknowledgements

Any opinions, findings, and conclusions or recommendations expressed in this article are those of the authors and do not necessarily reflect the views of the NSF.

Funding

This work was supported by the National Science Foundation (NSF) under Grant No. CMMI-1000667.

References

- Allen JJ and Smits AJ (2001) Energy harvesting Eel. *Fluids and Structures* 15: 629–640.
- Baerta K, Gyselinckx B, Torfsa T, et al. (2006) Technologies for highly miniaturized autonomous sensor networks. *Microelectronics Journal* 37: 1563–1568.
- Barrero-Gil A, Alonso G and Sanz-Andres A (2010) Energy harvesting from transverse galloping. *Journal of Sound and Vibration* 329: 2873–2883.
- Bibo A, Li G and Daqaq MF (2010) Electromechanical modeling and normal form analysis of a self-excited micro-power generator. *Journal of Intelligent Material Systems and Structures* 22: 577–592.

- Bryant M and Garcia E (2011) Modeling and testing of a novel aeroelastic flutter energy harvester. *Journal of Vibrations and Acoustics* 113: 011010.
- De Marqui C, Erturk A and Inman DJ (2010) Piezoaeroelastic modeling and analysis a generator wing with continuous and segmented electrodes. *Journal of Intelligent Material Systems and Structures* 21: 983993.
- Dunnmon JA, Stanton SC, Mann BP, et al. (2011) Power extraction from aeroelastic limit cycle oscillations. *Journal of Fluids and Structures* 27: 1182–1198.
- Erturk A, Vieira WGR, De Marqui C, et al. (2010) On the energy harvesting potential of piezoaeroelastic systems. *Applied Physics Letters* 96: 184103–184105.
- Fletcher NH (1992) Autonomous vibration of simple pressure-controlled valves in gas flows. *Journal of Acoustic Society of America* 93: 2172–2180.
- Hilaire AOST (1976) Analytical prediction of the non-linear response of a self-excited structure. *Journal of Sound and Vibrations* 27: 185–205.
- Kinsey T and Dumas G (2008) Parametric study of an oscillating airfoil in a power-extraction regime. *AIAA Journal* 46: 1318–1330.
- Liao JC, Beal D, Lauder J, et al. (2003) Fish exploiting vortices decrease muscle activity. *Science* 302: 1566–1569.
- Lissaman P (1983) Low-Reynolds-number airfoils. *Annual Review in Fluid Mechanics* 15: 223–239.
- Ricot D, Causse R and Misdarris N (2005) Aerodynamic excitation and sound production of blow-closed free reeds without acoustic coupling: the example of the accordion reed. *Journal of Acoustic Society of America* 117: 2279–2290.
- Robbins WP, Morris D, Marusic I, et al. (2006) Wind-generated electrical energy using flexible piezoelectric materials. In: *Proceedings of 2006 ASME international mechanical engineering congress and exposition*, Chicago, IL, November 5, 2006.
- Simpson BJ, Hover FS and Triantafyllou MS (2008) Experiments in direct energy extraction through flapping foils. In: *Proceedings of the eighteenth international offshore and polar engineering conference*, Vancouver, BC, Canada July 6, 2008 pp.370–376.
- St Clair D, Bibo A, Sennakesavababu VR, et al. (2010) A scalable concept for micropower generation using flow-induced self-excited oscillations. *Applied Physics Letters* 96: 144103–144106.
- Tang L, Padoussis P and Jang J (2009) Cantilevered flexible plates in axial flow: energy transfer and the concept of flutter-mill. *Journal of Sound and Vibration* 326: 263–276.
- Tarnopolsky AZ, Fletcher NH and Lai JCS (2000) Oscillating reed valves – an experimental study. *Journal of the Acoustical Society of America* 108: 400–406.
- Tarnopolsky AZ, Lai J and Fletcher N (2001) Flow Structures generated by pressure-controlled self-oscillating reed valves. *Journal of Sound and Vibration* 247: 213–226.
- Zhu Q, Haase M and Wu CH (2009) Modelling the capacity of a novel flow-energy harvester. *Applied Mathematical Modelling* 33: 2207–2217.

Appendix I

Constants appearing in the equations of motion

The beam shown in Figure 1 has a density ρ^b , modulus of elasticity Y^b , length L_b , width W_b , and thickness t_b . Attached to the beam is a piezoelectric element that has a density ρ^p , modulus of elasticity Y^p , length L_p , width W_p , and thickness t_p . The piezoelectric element is polarized along the 31 directions and has a piezoelectric constant d_{31} and a permittivity ϵ_{33} . With these definitions, the constants appearing in equation (1) can be expressed as

$$\omega^2 = \int_0^{L_b} \phi(s)[YI(s)\phi''(s)]ds, \quad \Theta = \int_0^{L_b} \phi(s)\theta''(s)ds, \quad \mathcal{E} = W_b \int_0^{L_b} \phi(s)ds$$

where ϕ is the mass-normalized first modal shape of a cantilever beam, $\int_0^{L_b} \rho_b t_b W_b \phi^2(s)ds = 1$. The bending stiffness, electromechanical coupling, and piezoelectric capacitance are given by

$$YI(s) = \frac{1}{3}(W_b Y^b (h_b^3 - h_a^3) + W_p Y^p (h_c^3 - h_b^3)) \\ [H(s) - H(s - L_p)] + \frac{W_p Y^b t_b^3}{12} [H(s - L_p) - H(s - L_b)] \\ \theta(s) = \frac{-W_p Y^p d_{31}}{2t_p} (h_c^2 - h_b^2) [H(s) - H(s - L_p)] \\ C_p = \frac{e_{33} W_p L_p}{t_p}$$

respectively. Here, $H(s)$ is the heavy side function; h_a , h_b , and h_c are the thickness boundaries measured from the neutral axis of the beam as shown in Figure 1. The location of the neutral axis is determined relative to the bottom surface of the composite beam by recalling that stresses through the cross section must be in equilibrium. This yields

$$h_a = -\frac{1}{2} \frac{Y^b W_b t_b^2 + 2Y^p W_p t_p t_b + Y^p W_p t_p^2}{Y^b W_b t_b + Y^p W_p t_p} \quad (14)$$